PCCP

Accepted Manuscript

ROYAL SOCIETY OF CHEMISTRY

www.rsc.org/pccp

Journal Name

ARTICLE

Insights on structural and dynamical features of water at halloysite interfaces probed by DFT and classical Molecular Dynamics simulations†

Davide Presti,[a] Alfonso Pedone,*[a] Giordano Mancini,*[b] Celia Duce,[c] Maria Rosaria Tiné[c] and Vincenzo Barone[b]

Received 00th January 20xx,
Accepted 00th January 20xx

DOI: 10.1039/x0xx00000x

www.rsc.org/

Density functional theory calculations and classical molecular dynamics simulations have been used to investigate the structure and dynamics of water molecules on kaolinite surfaces and confined in the interlayer of a halloysite model of nanometric dimension. The first technique allowed us to accurately describe the structure of the Tetrahedral-Octahedral slab of kaolinite in vacuum and in interaction with water molecules and to assess the performance of two widely employed empirical force fields to model water/clay interfaces. Classical molecular dynamics simulations were used to study the hydrogen bond network structure and dynamics of the water adsorbed on kaolinite surfaces and confined into halloysite interlayer. The results are in nice agreement with the few experimental data available in literature, showing a pronounced ordering and reduced mobility of water molecules at the hydrophilic octahedral surfaces of kaolinite and confined in the halloysite interlayer with respect to water interacting with the hydrophobic tetrahedral surfaces and in the bulk. Finally, this investigation provides new atomistic insights on the structural and dynamical properties of water-clay interfaces, which are of fundamental importance for both natural processes and industrial applications.

Introduction

Halloysite is a clay mineral with stoichiometry $Al_2Si_2O_5(OH)_4 \cdot nH_2O$ formed by surface weathering of the kaolinite mineral, and constitutes one of the most abundant and industrially important minerals on Earth. Kaolinite and halloysite are both layered silicates where each layer consists of a sheet of corner sharing [SiO_4] tetrahedral (T) linked through a sheet of edge sharing [AlO_6] octahedral (O), terminated with hydroxyl groups (see Figure 1).[1]

In kaolinite, an interlayer of hydrogen bonds (H-bonds) between the hydroxyl terminated gibbsite face and the silica terminated face binds these layers, whereas in the hydrated form of halloysite an interlayer of nanoconfined water molecules is present between the Tetrahedral-Octahedral (TO) layers spaced by 10 Å.[2] This intercalated water is weakly bound and can be easily and irreversibly removed.[3]

Since the X-ray Powder Diffraction patterns of both structures are quite similar, experimentalists usually distinguish them from the particle shape. Kaolinite is usually associated to samples with platy particles,[4,5] and halloysite to tubular or cylindrical particles.[6,7]

Understanding water-kaolinite (halloysite) interactions and the structural and dynamical properties of water molecules confined within these minerals is of fundamental importance for both natural processes and industrial applications[8]. In fact, the diffusion of water through clay minerals and concrete is of prime interest to scientists involved in nuclear waste repositories[9] or in the construction industry, where the key for making durable composite materials with long service life is to limit their ability to transport fluids like water.[10]

The knowledge of basic interactions between water and kaolinite/halloysite minerals is also useful to understand and predict chemical-physical processes occurring in the atmosphere, where they are present as nanometric dust and can act as nucleating agents for the formation of ice particles, which in turn catalyze the formation of radicals responsible for ozone depletion.[11]

Surprisingly, although water plays a crucial role in controlling and affecting all the properties of halloysite and kaolinite, little is known about the chemical and physical properties of water associated with such minerals.

From the experimental side, valuable contributions were provided by Bordallo's group that investigated the dynamics of

[a] Dipartimento di Scienze Chimiche e Geologiche, Università di Modena e Reggio-Emilia, via G. Campi 103, I-41125 Modena, Italy.
[b] Scuola Normale Superiore di Pisa, Piazza dei Cavalieri 7, I-56126 Pisa, Italy.
[c] Dipartimento di Chimica e Chimica Industriale, Università di Pisa, via Moruzzi 13, I-56124, Pisa, Italy.

†Electronic Supplementary Information (ESI) available: Potential parameters for the ClayFF and the PMMCS force fields; assessment of structural stability in the Hal-single and Hal-10 systems, completed with RMSD values vs. time and probability distribution for Al, Si and O atoms; parameters used in the hydrogen bond analysis. See DOI: 10.1039/x0xx00000x

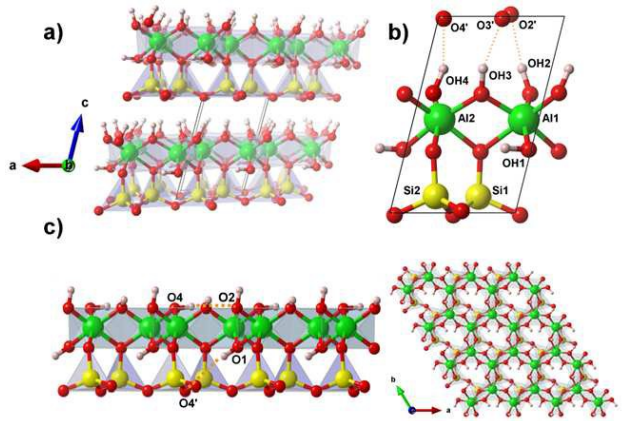

Figure 1. (a) Perspective and (b) orthographic views of kaolinite (B3LYP-D*) from the *ac* plane. The black line represents the unit cell, whereas the dashed orange lines represent the interlayer H-bonds. (c) View along the *b* axis (left) and *ab* plane (right) of a single layer of kaolinite (B3LYP-D* geometry). The polyhedra highlight octahedral and tetrahedral coordination sites belonging to Al (green) and Si (yellow) atoms, respectively.

confined water in hardened ordinary Portland cement paste,[10] montmorillonite and halloysite,[12] by means of Quasi-Elastic Neutron Scattering measurements.

In the first case, they were able to distinguish three different water interactions that is, water chemically bound into the paste, the so called 'glassy' water that physically interacts with the surfaces of the pores and unbound water molecules that are confined within large pores. They differentiated the stochastic reorientations of the water molecules occurring on the picosecond time scale to the diffusive motion ($D = 0.6\text{-}2\cdot10^{-9}$ m^2/s) of 'glassy' and 'unbound' water occurring in extended time scales (from hundredths of ps to a few ns).

In the subsequent work, focused on montmorillonite and halloysite minerals, they highlighted the effect of cations on the dynamics of confined water molecules and discriminated the dynamics of surface water from interlayer water. Interestingly, they measured a diffusion constant of about 0.7 and $2.1\cdot10^{-9}$ m^2/s for interlayer and surface water molecules in halloysite, respectively, and found that water mobility is higher in montmorillonite because of the presence of intercalated cations.

Regarding the spatial organization of interlayer water, a few neutron diffraction experiments have been attempted for smectite-type clay minerals,[13] but not for halloysite and kaolinite. In this respect, computer simulation techniques such as Density Functional Theory (DFT) and Molecular Dynamics (MD) simulations can provide new perspectives and complementary information on the structure and dynamics of confined water in clay minerals; recently one such study was reported by et al. Shahriyari showing the properties of montmorillonite under basin conditions[14]

Periodic DFT calculations have been used in the past to shed light on the spatial organization of OH groups on kaolinite (001) and other oxide surfaces[15–17] and to investigate their interactions with a few water molecules.[18–23]

However, because of the high computational cost, quantum mechanical based methods do not allow to investigate systems containing more than a few hundred of atoms, and to probe water dynamics at long time. These inconveniences are overcome by classical Molecular Dynamics simulations based on accurate force fields.

The wettability of both kaolinite surfaces has been investigated by means of classical MD simulations by several authors,[24–26] finding that different structural orientation of water occurs in the two surfaces and that the water mobility decreases when interacts with the hydroxylated one.

Ice nucleation in thin water films on the (001) kaolinite surface was also investigated very recently by Cox et al.,[27] who observed many nucleation events in small systems made up by 192 water molecules on kaolinite surface of 13.2x15.6 $Å^2$, but none when bigger cells were employed.

Whereas the studies cited above focused on the wettability of kaolinite surfaces, the main aim of the present investigation is to study the unique properties of water confined in the interlayer of halloysite-10, and to discriminate the structure and dynamics of water molecules on both surfaces of a single TO slab of kaolinite.

In the first part of the paper, two force fields, that is the ClayFF[28] and PMMCS[29,30] force fields, have been validated against accurate B3LYP-D*[31] periodic calculations on the reproduction of the structures of bulk and surfaces of kaolinite and on the adhesion energy of water molecules on both sides of the kaolinite slab.

Based on these results, the ClayFF was selected and combined with SPC-type[32] explicit water model to investigate water dynamics on kaolinite surfaces and in halloysite-10 at long time scale, using classical Molecular Dynamics.

Computational Details

Ab initio calculations. The starting ab initio quantum mechanical (QM) self-consistent calculations were carried out by using the CRYSTAL09 package,[33,34] which is based on an LCAO all-electron Gaussian basis-set approach, defined within the framework of periodic boundary conditions (PBC).

The bulk structure of kaolinite, as well as a single TO slab of kaolinite – with and without adsorbed water molecules – were fully relaxed at the B3LYP-D*/pob_TZVP level. The -D*[31] consists of a modified version of the -D2 pairwise potential of Grimme,[35] especially devised to take into account for dispersive interactions in molecular solids when coupled with the popular B3LYP functional.[36] Its general accuracy in describing the ground state structure of various kinds of organic and inorganic molecular solids has been widely demonstrated.[37–39] The triple-ζ pob_TZVP basis set optimized for solids is described in ref.[40]

By checking convergence on the total energy, we mapped the Irreducible Brillouin Zone (IBZ) with 112 *k*-points (keyword SHRINK 6 6).[34] The thresholds on exchange and coulomb integrals accuracy were set to: 10^{-9} 10^{-9} 10^{-9} 10^{-9} 10^{-18}. Default values have been used for the other input options.

The experimental kaolinite structure[1] was taken as initial structure for full geometry relaxation. A single TO slab of kaolinite was then generated from the relaxed bulk structure and further refined (full optimization of surface lattice constants and of atomic positions).
The water/kaolinite adhesion energies (corrected for the basis-set superposition error – BSSE – through the counterpoise (CP) method)[41] were obtained by absorbing one water molecule on different sites present in both tetrahedral and octahedral surfaces.

MM calculations. Classical molecular mechanics (MM) full relaxations were carried out by using the software GULP 4.0.[42] The force fields (FFs) adopted to model the system under investigation are the ClayFF[28] and the PMMCS.[29] All the interatomic potentials are reported in Tables S1 and S2 of the Electronic Supplementary Information (ESI).
The B3LYP-D* optimized structures obtained from the above calculations were used as input for full MM relaxations.

Molecular dynamics simulations of water-kaolinite (halloysite) interfaces. Figure 2 shows (a,b) the Halloysite-10 (Hal-10) and (c) the octahedral surface of the kaolinite slab (Hal-single) models investigated.
The Hal-10 model consists of 13090 atoms and it was built by stacking up two TO slabs generated by using 64 cells (1088 atoms) each with a distance between the two of 10 Å. The interlayer delimited by the octahedral surface of the first layer and the tetrahedral surface of the second one was filled up with 140 water molecules at random positions, in order to have a water density close to 1 g/cm^3. In this way, the number of water molecules per unit cell (2.2) is very close to that determined by Bordallo et al. (2.0).[12] The system was then inserted in a triclinic simulation box of 41.14 Å x 41.67 Å x 90.00 Å and filled up with water molecules. The Hal-single model was formed by a single TO slab of kaolinite, constituted by 900 unit cells (15300 atoms) and simulated in a triclinic box with sides of 152.9 Å x 156.2 Å x 90.0 Å, filled up with 57430 water molecules. The ClayFF force field, in conjunction with the SPC water model,[43] was adopted to model clay and water atoms. A second set of simulations of the Hal-10 system was also carried out for purpose comparison suing the SPC/E[44] water model.
Before the MD simulations, the energy of both models was minimized using a conjugate gradient procedure for 10^4 steps. Subsequently, four MD runs of 250000 steps each were carried out with integration time steps of 0.05 fs (at 50.00 K), 0.1 fs (at 100.00 K), 0.5 fs (at 298.15 K) and 1.0 fs (at 298.15 K) by using the GROMACS package[45] in a NVT ensemble. The velocity rescale thermostat[46] was used with a coupling constant of 0.1 ps). A fifth, 5 ns long (5000000 steps), equilibration run was performed in a NPT ensemble at 298.15 K and 1 bar (using the Parrinello-Rahman barostat[47] with a coupling constant of 2.0 ps) Finally, a production run of 20.0 ns (δt = 1.0 fs) was carried out in a NVT ensemble, saving coordinates every 250 steps, and updating the neighbour list every 10 steps; the Hal-10-SPC/E simulation was 10 ns long. The Particle Mesh Ewald method[48] (PME) was employed to describe long range electrostatics, and a cut-off of 12 Å was used for electrostatic and van der Waals interactions.
Radial distribution functions and Root Mean Square Deviations were calculated using standard definitions[49]. Residence times were evaluated using a modified version (see below) of the Impey's method:[50] to evaluate water/water residence time

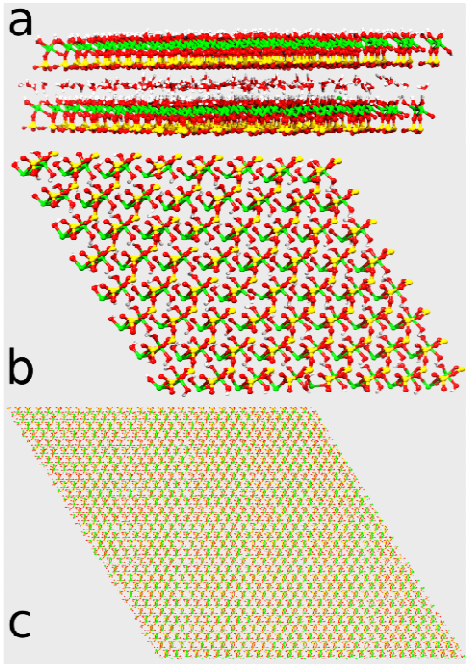

Figure 2. Graphical depictions of the **Hal-10** and **Hal-single** systems, studied by MD. (a) side view of the **Hal-10** system; the water molecules located between the two kaolinite TO slabs are shown in licorice. Only a reduced number of bonds is drawn. (b) bottom view (tetrahedral surface) of the lower TO slab of the **Hal-10** system. (c) top view (octahedral surface) of the **Hal-single** system.

within selected distances from the clay surface, an additional buffer time *t''* was used to check if a given water molecule was within this allowed zone when it was considered "as a solute" in the preceding definition. The buffer time *t** was always set to 2.0 ps while *t''* was estimated calculating residence times with respect to the clay atoms. Diffusion coefficients were evaluated performing a linear regression of Mean Square Displacement, using the Einstein's relation[51]. To analyse hydrogen bond dynamics, we used the continuous function devised by Pagliai et al.[52] over a simpler geometrical criterion. In this method, every donor—acceptor pair can be considered an hydrogen bond only partly, with a "score" between 0 and 1 given by:

$$f(r,\theta) = g(r; r_g, r_{HW}) \times g(\theta; \theta_g, \theta_{HW})$$

where r is the acceptor-hydrogen distance, θ the hydrogen–donor–acceptor angle, and

$$g(x; x_g, x_{HW}) = \begin{cases} 1 & if\ x \le x_g \\ e^{-(x^2 - x_g^2)/2x_{HW}^2} & if\ x > x_g \end{cases}$$

Here x_e and x_{hw} are the maximum and half-width values of either the radial or angular distribution function, obtained by fitting the left half of the corresponding distribution with a Gaussian curve. Data analysis was performed using an in house written Python codes based on Numpy (version 1.9, www.numpy.org) and the multiprocessing Python library. Plots have been obtained with the Grace program and images were created using the VESTA[53] and UCSF Chimera[54] packages.

Results and discussion

Quantum mechanical calculations and Force Fields validation.

Kaolinite Bulk. The primitive cell of kaolinite optimized at the B3LYP-D* level is shown in Figure 1a, whereas Table 1 reports the optimized lattice parameters of the primitive cell. The cell lattice parameters are compared with those computed previously (at the B3LYP[15] and B3LYP-D*[16] level) and with the experimental ones.[1] As expected, B3LYP functional provides lattice vectors overestimated of 1.1%-1.2%, whereas B3LYP-D* calculations give a better agreement with the *a* and *b* lattice parameters, overestimated of 0.3%-0.8%, and the *c* parameter underestimated of -1.0%. The variations between our B3LYP-D* calculations and the previous B3LYP-D* ones are probably due to the different basis-sets adopted.

Both the classical force fields yield, in general, to a well comparison with experiment and consequently, also with B3LYP-D* structures. However, the ClayFF – designed specifically to model clay minerals – leads to large deviations on lattice vectors (-0.5% to -1.4%) that compensate each other, resulting in a -0.4% deviation of the cell volume.

The PMMCS, instead, performs better along *b* and *c*, while a major underestimation (-1.7%) of the angle *α* takes place. PMMCS yields a cell slightly more compressed than the experimental one and, with the exception of the parameters *a* and *α*, it well reproduces our B3LYP-D* structure.

Table S3 of the ESI reports the OH bond distances, and the ones related to the interlayer H-bonds (oxygen-oxygen distances are given) computed at the different levels of theory. The DFT optimizations achieve a good prediction of both bonding and non-bonding distances. However, the B3LYP H-bond distances are slightly more accurate than the B3LYP-D* ones. This is not surprising since it is known that B3LYP provides good H-bond distances.[55] Between the two force fields used, the PMMCS performs slightly better than the CLAYFF, since the latter tends to underestimate H-bond distances.

Table S3 also reports the Al-O and Si-O bond distances and shows that the deviations from experimental data are small, at both DFT and MM level. Here, PMMCS gives slightly larger errors than ClayFF. Since such bonding parameters are well reproduced by all methods, and they do not present large variations when comparing the bulk solid and the TO slab surface (see e.g. Ref.[15]), they will not be commented further.

Kaolinite slab. The fully optimized B3LYP-D* structure of a single layer of kaolinite is depicted in Figure 1c. As it can be expected, in this case there are some structural differences with respect to the same layer included within kaolinite. The surface relaxation in vacuum markedly changes the displacement of outer hydrogen atoms, yielding to an *intra*layer H-bond (OH4···O3). Even the inner O(H)1 hydrogen undergoes to a severe rotation downwards from its position within the crystalline kaolinite (see Figure 1b for comparison), that leads to the formation of another H-bond with a tetrahedral oxygen (O4').

Table 2 shows that the PMMCS force field is, in general, more accurate than the ClayFF in reproducing the B3LYP-D* structural parameters of the slab, especially the bonding ones. The two angles – O4-H4-O2 and O1-H1-O4' – are predicted with large deviations from B3LYP-D* (from ca. 12° to ca. -34°), excepted for the ClayFF O4-H4-O2 (0.91°). However, OH···O distances are very well predicted. These latter are comparable, between the two H-bonds, whereas the related angles show that such kind of interactions are not perfectly straight. This underlines the medium-weak character of the mentioned H-bonds.

Water molecules adsorbed on the kaolinite TO slab. In this section, we report the results about water molecules adsorption on three different sites of the TO layer of the kaolinite mineral: (i) the SiO-1 site (Figure 3a), (ii) the AlO-1 site (Figure 3b), and (iii) the AlO-2 site (Figure 3c). The displayed structures are those fully optimized at the B3LYP-D* level. Since we are interested in the water-kaolinite (halloysite) interaction energy, and in the related H-bonds contacts, the intramolecular parameters are not commented. However, it is possible to notice that, in all the three cases, the outer hydrogen atoms (highlighted by blue circles in Figure 3a) belonging to the same OH groups are skewed along *b*, compared to the bare surface depicted in Figure 1c.

Journal Name

ARTICLE

Table 1. Computed (full geometry optimizations) and experimental lattice parameters and cell volume of the primitive cell of kaolinite (percentage relative deviations in parentheses). Data are reported in Å and degrees. Experimental parameters of the conventional cell (C_1 space group) are also reported in parentheses (last column).

	ClayFF	PMMCS	B3LYP-D* [a]		B3LYP-D* [b]	B3LYP [c]	Exp.[d]
a	5.143 (-0.5)	5.134 (-0.7)	5.206 (0.7)		5.184 (0.3)	5.230 (1.2)	5.17 (5.15)
b	5.210 (1.2)	5.164 (0.3)	5.192 (0.8)		5.190 (0.8)	5.210 (1.2)	5.15 (8.94)
c	7.299 (-1.4)	7.322 (-1.0)	7.323 (-1.0)		7.396 (-0.1)	7.480 (1.1)	7.40 (7.40)
α	84.08 (-0.2)	82.82 (-1.7)	84.08 (-0.2)		83.50 (-0.9)	84.10 (-0.2)	84.23 (91.69)
β	98.97 (0.3)	99.52 (0.8)	99.05 (0.4)		99.80 (1.1)	98.80 (0.1)	98.70 (104.61)
γ	60.40 (0.8)	60.12 (0.3)	59.89 (-0.1)	59.90 (0.0)	59.90 (0.0)	59.92 (89.82)	
Vol.	164.23 (-0.4)	161.04 (-2.4)	165.20 (0.1)	165.00 (0.0)	170.30 (3.2)	164.96	

[a] this work.; [b] from Ref.[16]; [c] from Ref.[15]; [d] from Ref.[1]

Table 2. Fully optimized parameters for the kaolinite surface. Data are reported in Å and degrees. The absolute deviations are given in parentheses with respect to our B3LYP-D* optimized structure (last column).

	ClayFF	PMMCS	B3LYP-D*
a	5.137 (0.003)	5.087 (-0.047)	5.134
b	5.224 (0.021)	5.201 (-0.002)	5.203
γ	119.50 (-0.17)	119.73 (0.06)	119.67
OH1	1.025 (0.065)	0.954 (-0.006)	0.960
OH2	1.025 (0.064)	0.949 (-0.012)	0.961
OH3	1.022 (0.063)	0.953 (-0.006)	0.959
OH4	1.022 (0.058)	0.958 (-0.006)	0.964
OH4-O2	2.252 (-0.188)	2.249 (-0.191)	2.440
O4-H4-O2	149.33 (0.91)	160.71 (12.29)	148.42
OH1-O4'	2.621 (0.247)	2.312 (0.062)	2.374
O1-H1-O4'	134.21 (-34.39)	152.26 (-16.34)	168.60

The computed water-kaolinite TO slab adhesion energies are reported in Table 3. The negative sign confirms that the transformation of kaolinite towards the halloysite mineral is a process thermodynamically favoured. The results confirm the bounty of the ClayFF force field in predicting adhesion energies with great accuracy with respect to B3LYP-D*. Notwithstanding the PMMCS furnishes good estimates for both intra- and inter- molecular distances (*vide infra*, Table 4), it severely over binds the water molecules onto the three surfaces. This is a direct consequence of the higher charges beard by atoms in the PMMCS FF ($Si^{+2.4}$,$Al^{+1.8}$, $O^{-1.2}$) with respect to the ClayFF ($Si^{+2.1}$, $Al^{+1.57}$, $O^{-1.05}$, etc.). To better match the adhesion energies relative to the water/TO slab interactions, the PMMCS should be screened by a fine tuned constant, as done in a previous work.[56]

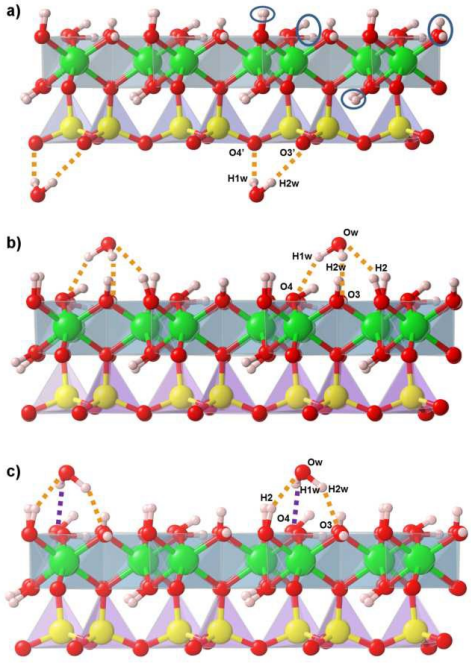

Figure 3. View along the *b* axis of the adsorption sites (a) **SiO-1** (b) **AlO-1** (c) **AlO-2** (B3LYP-D* geometry) – two supercells are depicted for convenience. The same labelling as in Fig. 1 is given. H-bonds with water molecules are highlighted in orange – also the existence of a weak H1w-O4 interaction (violet) is supposed. Skewed atoms are evidenced by blue circles in panel (a).

Because of the over binding, the PMMCS H-bond angles (Table 4) markedly deviate with respect to B3LYP-D*, especially on the SiO-1 site. The structural parameters concerning the water adsorption on the two Al sites are well described by both the FFs. Since the ClayFF provides very good adhesion energies and fair H-bond distances, it will be used to investigate the water-kaolinite (halloysite) interface.

Table 3. Adhesion energies (eV) of one water molecule on the 2x2x1 layer of kaolinite for the three adsorption sites. B3LYP-D* data are BSSE corrected.

	ClayFF	PMMCS	B3LYP-D*
SiO-1	-0.19	-0.64	-0.19
AlO-1	-0.63	-1.26	-0.70
AlO-2	-0.67	-1.20	-0.66

Table 4. Fully optimized H-bond distances and angles for water adsorption on kaolinite. Data are reported in Å and degrees. Absolute deviations are given in parentheses with respect to our B3LYP-D* optimized structure (last column).

	ClayFF	PMMCS	B3LYP-D*
SiO-1 site			
H1w-O4'	2.060 (-0.083)	2.194 (0.051)	2.143
H2w-O3'	2.075 (-0.103)	2.210 (0.032)	2.178
Ow-H1w-O4'	157.63 (-5.84)	152.32 (-11.15)	163.47
Ow-H2w-O3'	156.41 (-4.05)	151.06 (-9.40)	160.46
AlO-1 site			
Ow-H2	1.858 (-0.149)	2.106 (0.099)	2.007
H1w-O4	1.890 (-0.100)	1.897 (-0.093)	1.990
H2w-O3	2.075 (-0.103)	1.854 (-0.133)	1.987
Ow-H2-O2	148.97 (2.03)	143.21 (-3.73)	146.94
H1w-O4	142.70 (-1.39)	142.95 (-1.14)	144.09
H2w-O3	150.60 (5.34)	147.72 (2.46)	145.26
AlO-2 site			
Ow-H2	1.877 (-0.150)	2.783 (0.756)	2.027
H1w-O4	2.009 (-0.113)	1.921 (-0.201)	2.122
H2w-O3	1.780 (-0.175)	1.867 (-0.088)	1.955
Ow-H2-O2	141.53 (-1.65)	129.20 (-13.98)	143.18
Ow-H1w-O4	134.02 (-3.27)	144.76 (7.48)	137.29
Ow-H2w-O3	151.07 (0.62)	152.98 (2.53)	150.45

Molecular Dynamics study of the water-kaolinite (halloysite) interface.

Kaolinite (halloysite) structure. The stability of the TO slab in the Hal-single and Hal-10 systems in aqueous solution, along the simulation, was evaluated by computing the Root Mean Square Deviations (RMSD) of heavy atoms with respect to their starting positions and it is fully discussed in Section S1 of the Electronic Supplementary Information. Overall, the clay structure was very stable in both the Hal-single and Hal-10 systems showing very little deviations (up to 0.38 Å) and no signs of drift in the RMSD plots.

The water-halloysite interface. After having assessed the stability of the clay structure, the interactions between clay atoms and neighbour water molecules were studied to investigate the ordering or disordering effect of the TO slabs on water structure and dynamics.

An accurate description of the water structure near the clay surface in the Hal-single system was obtained by calculating oxygen-oxygen ($g_{OO}(r)$) and oxygen-hydrogen ($g_{OH}(r)$) radial distribution functions (RDFs) between water and the oxygen atoms on the Al (OH2, OH3, OH4) and Si (O2', O3', O4') faces of the TO slab. The results for the Al face are summarized in Figure 4a and 4b.

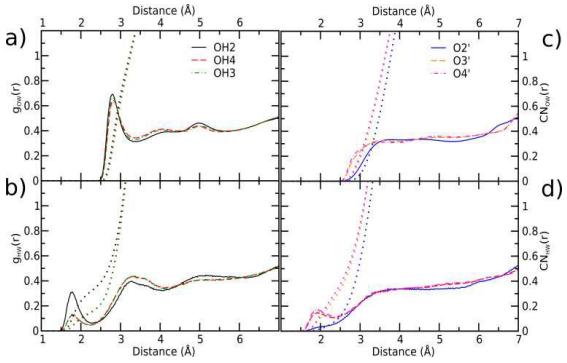

Figure 4. Radial distribution functions for the **Hal-single** system. (a) oxygen-oxygen (water) *g(r)* for atoms OH2, OH3 and OH4; the corresponding running integrals are shown as dotted lines. (b): oxygen-hydrogen (water) *g(r)* and running integrals. (c): oxygen-oxygen (water) *g(r)* for atoms O2', O3' and O4' atoms; running integrals are shown as dotted lines. (d): oxygen-hydrogen (water) *g(r)* and running integrals.

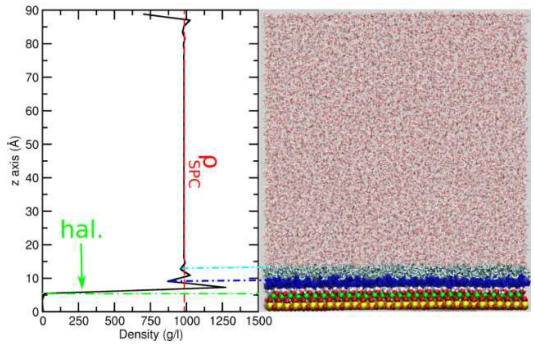

Figure 5. (a) Solvent density along the *z* axis in the **Hal-single** system. The dashed red line represents the density of SPC water (985 g/l), while the dot dashed blue line shows the limit of the clay slab at about 6 Å. (b) final snapshot of the simulation; the clay atoms are show as vdW spheres in the bottom part (yellow: Si atoms; green: Al atoms); water layers within the first (9.2 Å, blue) and the second (12.8 Å, cyan) minimum are shown with licorice representations of decreasing thickness.

The three hydroxyl groups feature comparable RDFs and running integrals with a first maxima at 2.8 Å (OH2) or 2.82 Å (OH3 and OH4), followed by a minimum at 3.35 Å, where a coordination number of 1 is reached. Despite their similarity, it is worth to observe that the OH2 curve (in black) features slightly higher (lower) maxima (minima). This can be better understood by looking at $g_{OH}(r)$ plots, where the different properties of OH2, as compared to OH3 and OH4, can be easily addressed. Even if the first maxima are located at the same position, the black curve corresponding to the OH2 features a much higher first peak (1.75 Å), and thus a higher coordination number before the first minimum (at 2.25 Å). The analysis of the water/oxygen radial distribution functions of the O2', O3' and O4' atoms yields to completely different results (see Figure 4c and 4d): no or very little structure is shown by $g_{OO}(r)$ and $g_{OH}(r)$, confirming the hydrophobic nature of the silica face exposed, and to the consequently less structured first water layer nearby the surface.

The coordination of water molecules on the octahedral surface of the Hal-single system creates an ordering effect of water

molecules near the clay. This can be better observed by the calculated density of water molecules along the *z* axis of the box in 50 bins of equal width (Figure 5a and 5b).

The solvent layers nearest to the Al surface show density deviations from the literature value of pure SPC water in NVT conditions (i.e. 985 g/l, see red dashed line) up to 250 g/l. The water column above the TO clay slab features two clearly observable minima at 9.2 (density of 860 g/l) and 12.8 Å (density of 960 g/l) that may correspond to solvent layers separated from the bulk solvent. In comparison, the effect induced by the silica layer (see top of Figure 6) on liquid water is much less relevant, featuring a single weakly pronounced minimum. Comparable results on the ordering of water atop kaolinite surface have also been obtained by Warne et al.[25]

Based on the results of the density analysis along *z*, 2D density maps of water oxygen atoms have been calculated partitioning the solvent in two slices going from 6.0 Å to 9.2 Å, and from 9.2 Å and 12.8 Å (see Figure 6a-b and 6c).

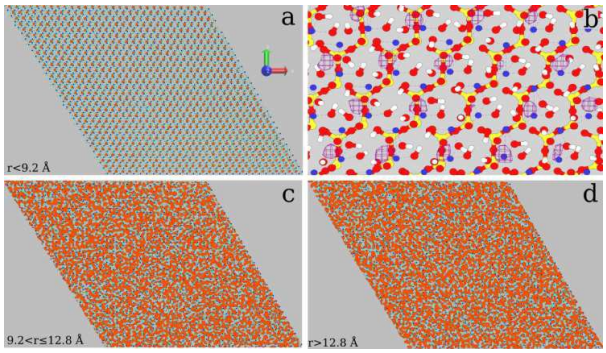

Figure 6. Density maps of oxygen atoms from water molecules within fixed cut-off along the *z* axis in the **Hal-single** system. (a) density map of oxygen atoms within 9.2 Å. The density isosurface is shown in orange-red, the Si and silica oxygen atoms with green wires, the Al atoms with blue spheres and the bridging oxygens and hydroxyl groups with cyan wires. (b) zoom of panel (a), representing a rectangular patch composed of 24 elementary cells. Clay atoms are represented using standard colors with the exception of Al (in blue); a reduced number of chemical bonds is shown for sake of simplicity. The oxygen density isosurface is depicted with purple wireframe. (c) Density map of oxygen atoms within 12.8 Å and (d) density map of oxygen atoms beyond 12.8 Å (bulk solvent). The colours correspond to those used in panel (a).

A third density map with z > 12.8 Å (more precisely, 50 ≤ *z* < 60 Å) was also generated for comparison with the bulk solvent.

The presence of the clay creates a sharp ordering effect in the first layer, that can easily be observed in Figures 6a and 6b; in contrast, there are minimal differences between Figures 6c and 6d, implying that the structure of the second layer is more similar to bulk water. Figure 6b shows that the oxygen density maximum tend to be located near the OH3 and OH2 groups, right above atom OH1, likely due to the underlying presence of highly charged Al atoms.

Liquid water structure in halloysite-10. Analysis of density oscillations along the *z* axis for the Hal-10 system (Figure 7) shows, on the "external faces", a separation between the first shell and bulk water similar to that obtained for the Hal-single system. The pattern observed on the octahedral upper surface is comparable to that observed in Figure 5 with sharper oscillations (up to 350 g/l). The water molecules in the inner layer exhibit a single maximum at 7.2 Å, mildly slanted toward the lower slab bearing the OH groups. The same analysis performed with the SPC/E water model yielded qualitatively comparable results. The inner water layer showed the a peak in the same position (7.21 Å), while the first (at 18.2 Å) and second peaks (at 22.3 Å) where located at slightly shorter distances as compared with SPC results (see Figures 7 and S4). Density oscillations above the upper layer were comparable to SPC (up 370 g/l) however the density peak of water between the two layers is much sharper and higher (1400 g/l as compared to 1200 g/l for SPC) indicating a more ordered inner water layer. Calculation of the average angle between the z-axis and water dipole moment in the same 50 bins (Figure 7 and S5 in the ESI) showed that the first two shells above the upper layer had a small persistent anisotropy (cos(θ) = ±0.15) compatible with water molecules oriented with one OH bond perpendicular to the halloysite sheet. An increased deviation from a random orientation was observed in in the halloysite interlayer, with deviations up to 25° and the formations of two antiparallel water layers.

A more detailed description of the hydration structure is also obtained by means of radial distribution functions reported in Figure 8. The external faces of the Hal-10 system, i.e. the octahedral surface of the upper slab and the tetrahedral

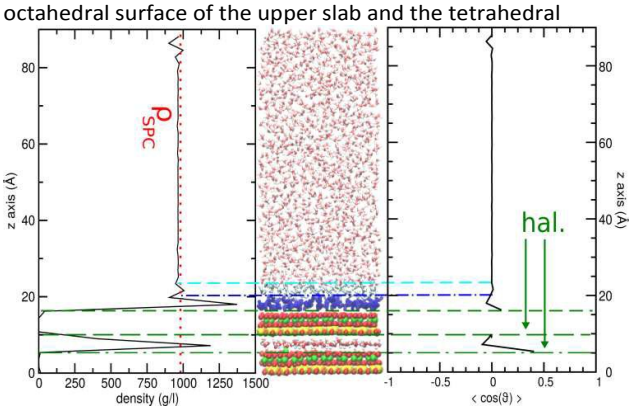

Figure 7. (left) Solvent density along the *z* axis in the **Hal-10** system. The dashed red line represents the density of SPC water (985 g/l), while the dashed green lines show the limits of the upper and lower clay slab. (right) Final snapshot of the simulation; the clay atoms are show as vdW spheres in the bottom part (yellow: Si atoms; green: Al atoms); water layers on the octahedral face of the upper slab within the first (19.7 Å, blue) and the second (22.9 Å, cyan) minimum are shown with licorice representations of decreasing thickness. (c) orientation of water molecules in the box. The average cosine of the z axis/ water dipole moment angle is shown

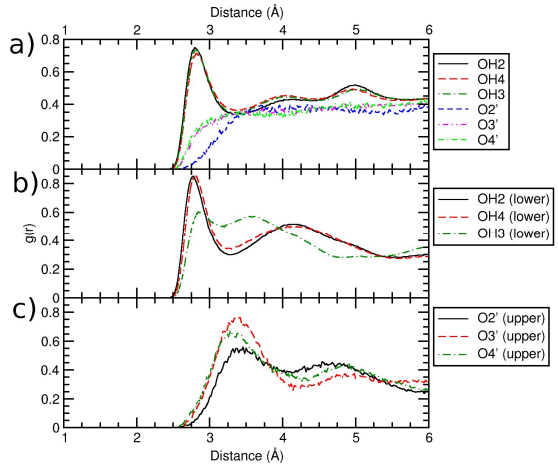

Figure 8. Oxygen-oxygen radial distribution functions for the **Hal-10** system. (a) Results obtained for the octahedral surface of the upper slab and the tetrahedral surface of the lower slab. (b) Results obtained from the trajectory of oxygen atoms on the octahedral surface of the lower slab. (c) Results obtained from the trajectory of oxygen atoms on the tetrahedral surface of the upper slab.

surface of the lower slab, share the same first maximum and minimum positions (Figure 8a) found when analysing the Hal-single trajectory (Figure 4). Instead, the water molecules confined between the two kaolinite layers present a different structure. The $g(r)$ of the OH2 and OH4 groups on the octahedral surface of the lower slab (Figure 8b) show a first/second solvation shell separation similar to that obtained for the upper slab and for the Hal-single system, even though the first peak is narrower (FWHM of 0.36 Å vs. 0.42 Å) and the first minimum deeper (0.30 Å vs 0.35 Å).

Therefore, the water molecules confined in the halloysite interlayer assume a more ordered structure than those absorbed on the outer surface of the same type. The OH3 features a completely different distribution with two low, weakly separated maxima at 2.8 and 3.6 Å.

Differences are even more striking for the tetrahedral surface of the upper lying TO slab (Figure 8c), that presents a well-defined hydration structure with a first maximum of varying height located at 3.25 Å, and a weakly pronounced first minimum at 4.25 Å.

Following the analysis of the Hal-10 system hydration structure, we deeply investigated the hydrogen bond dynamics on the octahedral surface and into the interlayer of the Hal-10 system. H-bond formation was studied using the methodology described in the Section 'Computational Details'. The radial values r_e and r_{hw} were obtained from either the O_{clay}–H_{water} or H_{clay}–O_{water} $g(r)$ and θ_e and θ_{hw} were evaluated from the angular distribution functions (ADFs), thus analysing separately the ability of kaolinite hydroxyl groups to act either as donor or acceptors. Values for x_e and x_{hw} parameters for distances and angles are provided in Table S4 of the ESI.

Figures 9 and 10 show the analysis of hydrogen bonds formed by OH2, OH3 and OH4 groups on either slab (with water and between them) and by O2', O3' and O4' atoms on the upper slab. Although oxygen atom in the tetrahedral surface of the upper slab features some degree of structure (Figure 8c),

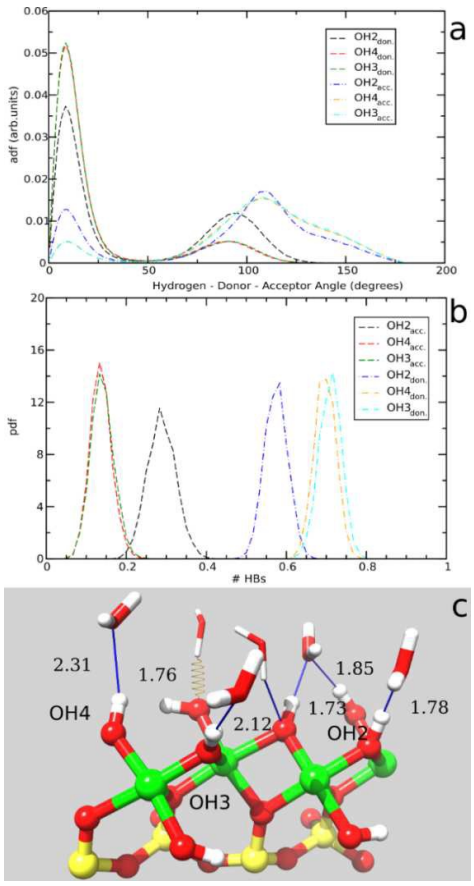

Figure 9. Hydrogen bonds (HBs) formed between atoms in the upper octahedral surface of the **Hal-10** system and water molecules. (a) Angular distribution functions for H-donor-acceptor angles for the OH2, OH3 and OH4 groups acting either as donors or acceptors. (b) Number of HBs formed by OH2, OH3 and OH4 groups acting either as donors or acceptors. (c) Representative snapshots of water coordination in the upper slab. Water molecules have been drawn using thick or thin sticks, depending on their orientation. HBs have been drawn as orange springs or blue rods, depending on whether the water molecule was acting as donor or acceptor. Distances are in Å; note that only a subset of distances is shown for the sake of simplicity.

calculation of ADF did not show any preferred value (data not shown) and a low average number of HBs (up to 0.4 for O4'); they were thus excluded from further analysis. Analogous results were also obtained in other MD studies of kaolinite.[26,57]

Figure 9a shows the average orientation of water molecules on upper octahedral surface. In agreement with previous investigations,[18,19,26], in particular classical[58] and ab-initio[21,23,59] MD studies of water nanofilms in halloysite systems, we observed that two preferred orientations exist for water molecules on the octahedral surface. In one of these, water molecules are oriented with one OH bond pointing directly towards the clay oxygen (H_2O is a donor in such case) while, in the other, the water oxygen points towards the clay atoms; for both orientations the first maximum is located approximately at 10°.

Hydroxyl groups in the upper layer yielded to a comparable number of H-bonds (about 0.85), but features a different propensity to act as donors or acceptors (Figure 9b). The

difference is relatively weak for OH2 (0.29 vs 0.56 H-bonds), while OH3 and OH4 tend to act almost exclusively as acceptors. This is in agreement with the density map of Figure 6b, where the maximum of water oxygen density is located above the OH2 group. A representation of such structures is given in Figure 9c, where six water molecules are bound to clay atoms, alternating between donors and acceptors: there are two of the former and four of the latter, in qualitative agreement with Figure 9b. An ordered low-density layer of water molecules is thus created on the clay surface, in agreement with the result of Figures 5 and 7, and with high residence times of the first shell water molecules observed in the Hal-single system.

Figure 10a displays the angular distributions functions for the OH2, OH3 and OH4 groups in the lower layer; overall, the results are very similar to those of the upper slab reported in Figure 9a. The average number of hydrogen bonds for the OH2, OH3 and OH4 groups is 0.87, 0.86 and 0.76, respectively, and it is comparable with the results obtained for the upper slab, with the exception of OH3, which has a decreased average number of H-bonds, with respect to the upper slab (0.83 vs 0.76) and to the other hydroxyl groups.

Our simulations show that OH2 can act either as donor or acceptor, while OH3 and OH4 have an higher propensity to act as acceptors of hydrogen bonds. The two orientation patterns observed in Figure 9c are also found in Figure 10c, with water molecules alternating their role.

Water (oxygen atoms) residence time in the first shell of either tetrahedral or octahedral surfaces of both layers as well as water/water first shell residence times for bulk water are shown in Table S5 in the ESI. Comparison of the results obtained with the SPC and SPC/E water models shows in general, longer exchange rates for SPC/E, in agreement with the reduced mobility reported for this model. Interestingly, the SPC/E vs SPC ratio between residence times among the same surface (e.g. upper tetrahedral/ lower tetrahedral) using either model oscillates between 1.44 and 1.55 very similar to the value obtained between the two models in bulk water (1.2); only for the intralayer water molecules the increase of residence time using SPC/E ($\tau_{SPC/E}/\tau_{SPC}$ = 1.25) is somewhat lesser than what could be expected with an extrapolation. It is worth to observe that employing the first shell residence time as buffer time to consider a water molecule in the first shell of a nearby clay atom, lateral swaps between water molecules were also analysed, and give a residence time comparable with that of bulk water (τ = 1.91 ps for SPC and 2.12 for SPC/E).

The water/water structure is also affected: an average of 1.07 hydrogen bonds per water molecule is present, while 1.75 HBs are observed on average in bulk SPC water. The water/water residence time (Table S5) is similar to the clay/water value, i.e. slightly below 20 ps. Water molecules within the inner layer feature both a highly reduced perpendicular exchange rate and a highly reduced lateral exchange rate. Calculation of the diffusion coefficient on the *xy* plane yielded to a value of 1.08 ± 0.15 × 10^5 cm^2 s^{-1} for such water molecules, as compared to 3.85× 10^5 cm^2 s^{-1} reported for SPC water.[60] The Hal-10-SPC/E simulation showed a similar behaviour, with D=1.02±0.16 × 10^5 cm^2 s^{-1} compared to the bulk value of SPC/E water[60] i.e. D=2.49 × 10^5 cm^2 s^{-1} and water/water.

These observations are in nice agreement with those determined by Bordallo et al. on montmorillonite and halloysite[12] by means of Quasi-Elastic Neutron Scattering measurements and confirm the reliability of our simulations.

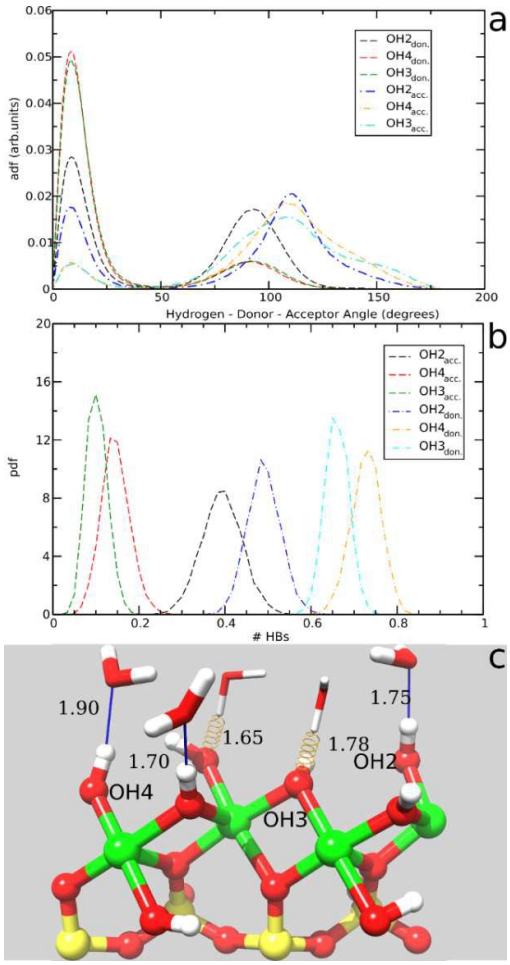

Figure 10. Geometry of water coordination on the kaolinite surface. (a) Angular distribution functions for H_{clay}-O_{clay}-OW and HW-O-O_{clay} obtained for the upper slab. (b) Number of HBs formed by OH2, OH3 and OH4 groups acting either as donors or acceptors. (c) Representative snapshots of water coordination in the upper slab. Water molecules have been drawn using thick or thin sticks, depending on their orientation. HBs have been shown as orange springs or blue rods, depending on whether the water molecule was acting as donor or acceptor. Distances are in Å; note that only a subset of distances is shown for the sake of simplicity.

Conclusions

Density functional calculations and classical molecular dynamics simulations have been used to study the structure and dynamics of water interacting with kaolinite surfaces and confined in the interlayer of halloysite-10.

As a necessary step of our computational approach, a preliminary assessment of the structural properties of kaolinite was carried out by means of accurate dispersion-corrected DFT

quantum and classical static calculations, within the frame of periodic boundary conditions. These involved the optimization of the kaolinite structure in its bulk form, a single kaolinite Tetrahedral-Octahedral (TO) slab and three hydrated forms of a single TO slab of kaolinite. Based on the bounty in reproducing the DFT structural parameters and water adhesion energies, the ClayFF force field was chosen to investigate the clay-water dynamics at long time scales.

For this purpose, two large systems have been considered: the Hal-single, constituted by a single dioctahedral layer of kaolinite interacting with water, and the Hal-10, constituted by two TO layers, 10 Å distant, with intercalated and external water molecules.

In solution, the external surfaces of both systems presented high stability, with no particular changes in the global structure of clay and water molecules.

However, analyses of the local structure of Hal-single and Hal-10 systems at long time unveiled that in the former model the water molecules weakly interact with the tetrahedral face, yielding less structured water/clay interfaces.

A pronounced molecular ordering of water takes place on the octahedral surfaces, where the residence time for vertical exchange of water molecules is markedly higher than for bulk water. In this case, structural features related to each interaction site permit a net distinction of the diverse terminal hydroxyl groups, especially from density deviations of oxygen atoms belonging to water, that are accompanied by disordered, faster vertical exchange of water molecules. Interestingly, the interfaces between the two internal surfaces of Hal-10 with water show more similar properties with respect to the external ones. In this system, water molecules undergo to a notable ordering at the Si-O/water sites, proven by their very low vertical and lateral exchange rates.

In conclusion, long time dynamics of water-kaolinite interactions yielded to a better understanding of the high stability of the intercalated water within halloysite and at the external Si-O surfaces. These findings can be useful to drive both the experimental and the computational research towards novel technological applications related to solvent adhesion and intercalation, based on naturally present materials as clay minerals.

Acknowledgements

A. P. thanks the University of Modena and Reggio-Emilia for supporting this work by granting the internal project (Fondo di Ateneo per la Ricerca, FAR2014) entitled “Role of modular phyllosilicates for the capture and storage of CO_2: an experimental and computational investigation”.

G. M. thanks Dr. Valentina Erastova for useful discussion and the DreamsLab technical staff for managing the computational facilities at SNS. This work was also supported by MIUR (FIRB project n° RBFR12ETL5 and PRIN project 2010C4R8M8_002).

Notes and references

1 R. B. Neder, M. Burghammer, T. Grasl, H. Schulz, A. Bram and S. Fiedler, *Clays Clay Miner.*, 1999, **47**, 487–494.
2 L. Guimarães, A. N. Enyashin, G. Seifert and H. A. Duarte, *J. Phys. Chem. C*, 2010, **114**, 11358–11363.
3 E. Joussein, S. Petit, J. Churchman, B. Theng, D. Righi and B. Delvaux, *Clay Miner.*, 2005, **40**, 383–426.
4 S. R. Levis and P. B. Deasy, *Int. J. Pharm.*, 2002, **243**, 125–134.
5 R. Klimkiewicz and E. B. Drąg, *J. Phys. Chem. Solids*, 2004, **65**, 459–464.
6 J. H. Kirkman, *Clay Miner.*, 1975, **10**, 475–478.
7 J. H. Kirkman, *Clay Miner.*, 1977, **12**, 199–216.
8 R. T. Cygan and K. Tazaki, *Elements*, 2014, **10**, 195–200.
9 R. Pusch, in *Developments in Clay Science*, ed. B. K. G. T. and G. L. Faïza Bergaya, Elsevier, 2006, vol. 1, pp. 703–716.
10 H. N. Bordallo, L. P. Aldridge and A. Desmedt, *J. Phys. Chem. B*, 2006, **110**, 17966–17976.
11 J. P. D. Abbatt, *Chem. Rev.*, 2003, **103**, 4783–4800.
12 H. N. Bordallo, L. P. Aldridge, G. J. Churchman, W. P. Gates, M. T. F. Telling, K. Kiefer, P. Fouquet, T. Seydel and S. A. J. Kimber, *J. Phys. Chem. C*, 2008, **112**, 13982–13991.
13 E. Ferrage, B. A. Sakharov, L. J. Michot, A. Delville, A. Bauer, B. Lanson, S. Grangeon, G. Frapper, M. Jiménez-Ruiz and G. J. Cuello, *J. Phys. Chem. C*, 2011, **115**, 1867–1881.
14 R. Shahriyari, A. Khosravi and A. Ahmadzadeh, *Mol. Phys.*, 2013, **111**, 3156–3167.
15 S. Tosoni, K. Doll and P. Ugliengo, *Chem. Mater.*, 2006, **18**, 2135–2143.
16 P. Ugliengo, C. M. Zicovich-Wilson, S. Tosoni and B. Civalleri, *J. Mater. Chem.*, 2009, **19**, 2564–2572.
17 A. Rimola, D. Costa, M. Sodupe, J.-F. Lambert and P. Ugliengo, *Chem. Rev.*, 2013, **113**, 4216–4313.
18 D. Tunega, L. Benco, G. Haberhauer, M. H. Gerzabek and H. Lischka, *J. Phys. Chem. B*, 2002, **106**, 11515–11525.
19 D. Tunega, M. H. Gerzabek and H. Lischka, *J. Phys. Chem. B*, 2004, **108**, 5930–5936.
20 D. Tunega, G. Haberhauer, M. H. Gerzabek and H. Lischka, *Langmuir*, 2002, **18**, 139–147.
21 X. L. Hu and A. Michaelides, *Surf. Sci.*, 2008, **602**, 960–974.
22 E. Berardo, A. Pedone, P. Ugliengo and M. Corno, *Langmuir*, 2013, **29**, 5749–5759.
23 X. L. Hu and A. Michaelides, *Surf. Sci.*, 2007, **601**, 5378–5381.
24 K. S. Smirnov and D. Bougeard, *J. Phys. Chem. B*, 1999, **103**, 5266–5273.
25 M. R. Warne, N. L. Allan and T. Cosgrove, *Phys. Chem. Chem. Phys.*, 2000, **2**, 3663–3668.
26 R. Šolc, M. H. Gerzabek, H. Lischka and D. Tunega, *Geoderma*, 2011, **169**, 47–54.
27 S. J. Cox, Z. Raza, S. M. Kathmann, B. Slater and A. Michaelides, *Faraday Discuss.*, 2014, **167**, 389–403.
28 R. T. Cygan, J.-J. Liang and A. G. Kalinichev, *J. Phys. Chem. B*, 2004, **108**, 1255–1266.
29 A. Pedone, G. Malavasi, M. C. Menziani, A. N. Cormack and U. Segre, *J. Phys. Chem. B*, 2006, **110**, 11780–11795.
30 A. Pedone, *J. Phys. Chem. C*, 2009, **113**, 20773–20784.
31 B. Civalleri, C. M. Zicovich-Wilson, L. Valenzano and P. Ugliengo, *Crystengcomm*, 2008, **10**, 405–410.
32 H. J. C. Berendsen, J. P. M. Postma, W. F. Van Gunsteren and J. Hermans, *Intermolecular Forces*, 1981, **11**, 331–342.
33 R. Dovesi, R. Orlando, B. Civalleri, C. Roetti, V. R. Saunders and C. M. Zicovich-Wilson, *Z. Krist.*, 2005, **220**, 571–573.
34 R. Dovesi, V. R. Saunders, C. Roetti, R. Orlando, C. M. Zicovich-Wilson, F. Pascale, K. Doll, N. M. Harrison, B. Civalleri, I. J. Bush, P. D’Arco, and M. Llunell, *CRYSTAL09 User’s Manual*, Università di Torino, Torino, 2010.
35 S. Grimme, *J. Comput. Chem.*, 2006, **27**, 1787–1799.
36 P. J. Stephens, F. J. Devlin, C. F. Chabalowski and M. J. Frisch, *J. Phys. Chem.*, 1994, **98**, 11623–11627.

37 D. Presti, A. Pedone, M. C. Menziani, B. Civalleri and L. Maschio, *Crystengcomm*, 2014, **16**, 102–109.
38 D. Presti, A. Pedone and M. C. Menziani, *Inorg. Chem.*, 2014, **53**, 7926–7935.
39 D. Presti, F. Labat, A. Pedone, M. J. Frisch, H. P. Hratchian, I. Ciofini, M. C. Menziani and C. Adamo, *J. Chem. Theory Comput.*, 2014, **10**, 5577–5585.
40 M. F. Peintinger, D. V. Oliveira and T. Bredow, *J. Comput. Chem.*, 2013, **34**, 451–459.
41 S. F. Boys and F. Bernardi, *Mol. Phys.*, 1970, **19**, 553–566.
42 J. D. Gale and A. L. Rohl, *Mol. Simul.*, 2003, **29**, 291–341.
43 H. J. C. Berendsen, J. P. M. Postma, W. F. van Gunsteren and J. Hermans, in *Intermolecular Forces*, ed. B. Pullman, Springer Netherlands, 1981, pp. 331–342.
44 H. Berendsen, J. Grigera and T. Straatsma, *J. Phys. Chem.*, 1987, **91**, 6269–6271.
45 S. Pronk, S. Pall, R. Schulz, P. Larsson, P. Bjelkmar, R. Apostolov, M. R. Shirts, J. C. Smith, P. M. Kasson, D. van der Spoel, B. Hess and E. Lindahl, *Bioinformatics*, 2013, **29**, 845–854.
46 G. Bussi, D. Donadio and M. Parrinello, *J. Chem. Phys.*, 2007, **126**, 014101.
47 M. Parrinello, *J. Appl. Phys.*, 1981, **52**, 7182.
48 T. Darden, L. Perera, L. Li and L. Pedersen, *Structure*, 1999, **7**, R55–R60.
49 A. R. Leach, *Molecular modelling: principles and applications*, Prentice Hall, Harlow, England ; New York, 2nd ed., 2001.
50 R. W. Impey, P. A. Madden and I. R. McDonald, *J. Phys. Chem.*, 1983, **87**, 5071–5083.
51 M. P. Allen and D. J. Tildesley, *Computer simulation of liquids*, Clarendon Press ; Oxford University Press, Oxford [England]; New York, 1989.
52 M. Pagliai, F. Muniz-Miranda, G. Cardini, R. Righini and V. Schettino, *J. Phys. Chem. Lett.*, 2010, **1**, 2951–2955.
53 K. Momma and F. Izumi, *J. Appl. Crystallogr.*, 2011, **44**, 1272–1276.
54 E. F. Pettersen, T. D. Goddard, C. C. Huang, G. S. Couch, D. M. Greenblatt, E. C. Meng and T. E. Ferrin, *J. Comput. Chem.*, 2004, **25**, 1605–1612.
55 A. Pedone, G. Malavasi, M. C. Menziani, U. Segre, F. Musso, M. Corno, B. Civalleri and P. Ugliengo, *Chem. Mater.*, 2008, **20**, 2522–2531.
56 A. Pedone, G. Prampolini, S. Monti and V. Barone, *Chem. Mater.*, 2011, **23**, 5016–5023.
57 T. Croteau, A. K. Bertram and G. N. Patey, *J. Phys. Chem. A*, 2009, **113**, 7826–7833.
58 N. R. Haria, G. S. Grest and C. D. Lorenz, *J. Phys. Chem. C*, 2013, **117**, 6096–6104.
59 P. J. Feibelman, *J. Phys. Chem. C*, 2013, **117**, 6088–6095.
60 M. W. Mahoney and W. L. Jorgensen, *J. Chem. Phys.*, 2001, **114**, 363.

TOC IMAGE